Soft Matter

PAPER

View Article Online
View Journal

Aggregation dynamics, structure, and mechanical properties of bigels

Cite this: DOI: 10.1039/c3sm52558a

L. Di Michele,*[a] D. Fiocco,*[b] F. Varrato,*[b] S. Sastry,[ce] E. Eiser[a] and G. Foffi*[d]

Recently we have introduced *bigels*, inter-penetrating gels made of two different colloidal species. Even if particles with simple short-range isotropic potential are employed, the selective interactions enable the tunability of the self-assembly, leading to the formation of complex structures. In the present paper, we explore the non-equilibrium dynamics and the phenomenology underlying the kinetic arrest under quench and the formation of bigels. We demonstrate that the peculiar bigel kinetics can be described through an arrested spinodal decomposition driven by demixing of the colloidal species. The role played by the presence of a second colloidal species on the phase diagram, as expanded to account for the increased number of parameters, is clarified both *via* extensive numerical simulations and experiments. We provide details on the realisation of bigels, by means of DNA-coated colloids (DNACCs), and the consequent imaging techniques. Moreover we evidence, by comparison with the usual one-component gel formation, the emergence of controllable timescales in the aggregation of the bigels, whose final stages are also experimentally studied to provide morphological details. Finally, we use numerical models to simulate the bigel response to mechanical strain, highlighting how such a new material can bear significantly higher stress compared to the usual one-component gel. We conclude by discussing possible technological uses and by providing insights on the viable research steps to undertake for more complex and yet tuneable multi-component colloidal systems.

Received 2nd October 2013
Accepted 17th January 2014

DOI: 10.1039/c3sm52558a

www.rsc.org/softmatter

1. Introduction

In the last two decades the understanding of colloidal gelation due to reversible attractive interactions posed a major challenge in soft matter research.[2] In the limiting case of extremely strong attraction between the colloids, and low volume fraction, gelation has been explained by means of diffusion limited cluster aggregation, as confirmed by computer simulations[3–8] and experiments.[9–12] For less strong attraction, and intermediate volume fractions, gelation has been shown to occur as a consequence of an arrested phase separation process.[13–21] Upon quenching a homogeneous colloidal "gas" from high to low temperatures, deeply within the liquid–liquid coexistence region of the phase diagram, any fluctuation in the local colloidal density grows rapidly, thus forming the peculiar spinodal patterns. When the dense regions reach a critical volume fraction, the high-density liquid becomes glassy and the spinodal decomposition is interrupted. The arrested phase separation leads to the formation of a percolating network that, despite exhibiting slow aging dynamics, is capable of bearing mechanical stress.

Even though this non-equilibrium route to colloidal gelation is accepted as universal for one-component systems,[13,14] a generalisation to multi-component mixtures is still required. When quenching binary colloidal mixtures with selective intra-species attraction, local composition fluctuations develop and cause the separation between the two components. Analogously to the one-component case, this *demixing* process can get arrested and lead to the formation of interpenetrating networks of the two components.[1] Under suitable conditions, both these networks are space spanning, forming what we call a *bigel*.

Having demonstrated the experimental feasibility of bigels by using DNA-coated colloids (DNACCs), many questions concerning the process of *arrested demixing* and the resulting mechanical response remain open. In this paper we provide a detailed characterisation of the demixing dynamics and the consequent structuration of binary colloidal mixtures with selective intra-species attraction and hard core inter-species repulsion. These systems are studied by means of molecular dynamics (MD) simulations and experimentally by using binary mixtures of DNACCs. We perform percolation analysis and morphological characterisation for samples with different

[a]University of Cambridge, Cavendish Laboratory, JJ Thomson Avenue, Cambridge CB3 0HE, UK
[b]Institute of Theoretical Physics, Ecole Polytechnique Federale de Lausanne, Lausanne 1015, Switzerland
[c]Jawaharlal Nehru Centre for Advanced Scientific Research, Jakkur Campus, Bangalore 560064, India
[d]Laboratoire de Physique de Solides, UMR 8502, Universite Paris-Sud, Bt. 510, Orsay F-91405, France. E-mail: giuseppe.foffi@u-psud.fr
[e]TIFR Centre for Interdisciplinary Sciences, 21 Brundavan Colony, Narsingi, 500075 Hyderabad, India

volume fractions and compositions by means of chord-distribution analysis[16,22,23] and other morphological observables, showing good agreement between computer simulations and experiments. The demixing dynamics is mainly investigated by looking at the time evolution of the static structure factor. By applying the Furukawa scaling,[24,25] we argue that the demixing process follows indeed the route of a spinodal decomposition, justifying the generalisation of the arrested phase separation framework to the gelation of binary colloidal mixtures.

In the final part of this article we provide preliminary evidence for the exceptional mechanical properties of bigels. By means of computer simulations, we demonstrate that the arrested phases yield at much higher shear stresses, upon continuous shearing, compared to one-component gels with the same solid content, which instead collapse.

To conclude we propose a possible extension of the discussed gelation mechanism to *n*-component systems that offer the possibility of further controlling the kinetics of arrested phase separation by sequentially activating selective interactions.[26] Such a control will enable the construction of arbitrarily complex mesoporous media. We also suggest possible technological applications of our strategy to battery materials, hybrid photovoltaics, and biomimetic photonic media.

2. Numerical investigation

2.1. Computer simulations model

We adopt a widely used model that encapsulates the properties of short-ranged attractive colloidal systems.[13,19,27] This model plays an important role in the investigation of colloidal gelation[19] as well as glass formation in denser systems.[28–31] Square-well (SW) potentials are used for the interactions between colloidal particles. By introducing different species (components), the multicomponent SW model takes the form

$$U_{ij}(r) = \begin{cases} +\infty & \text{if } r \le D \\ -\varepsilon_{ij} & \text{if } D < r \le \delta D \\ 0 & \text{if } r > \delta D \end{cases}, \quad (1)$$

where ε_{ij} represents a matrix that defines the interactions between components i and j, D is the diameter of the particles and δ gives the range of the interaction. The success of the SW model is due to its simplicity and to the fact that, when the range of the attraction is short, the relevant physical properties depend only weakly on the shape of the potential.[32] The SW model fulfills such a condition if the attraction range is $\delta - 1 \lesssim 5\%$ of the diameter. We fix $D = 1$ and $\delta = 1.03$, a value often used in MD simulations of square-well fluids, gels and glasses.[30,31,33] In our reduced units, the mass of all the particles is unity and the Boltzmann constant $k_B = 1$, so that the temperature is measured in terms of the well depth ε. Time is measured in units of $D\sqrt{m/|\varepsilon|}$ and the maximum length used for the runs is of 6.9×10^5 time units.

While the shape and size of all particles are the same, we allow for different interspecies interactions among different species of colloids. Here we limit ourselves to the case of two component mixtures (2CM) and, from now on, label the two species as R (red) and G (green), *i.e.* i, j = R, G, in order to compare the simulation results with our experimental data. For reference, we also simulate one-component (1CM) systems with $\varepsilon_{ii} = 1$. With the present choice, $T = 1$ corresponds to a thermal energy k_BT, equal to the attractive well depth.

For the 2CM attraction matrix, we choose the parameters $\varepsilon_{RR} = \varepsilon_{GG} = 1$ for the intra-species attraction, while the inter-species attraction is set to $\varepsilon_{RG} = 0$, reflecting pure hard-sphere (HS) repulsion among the two species. With this choice, in fact, we maximise the demixing, due to the composition fluctuations in competition with the (overall) density fluctuations.[1]

We use an Event Driven algorithm for the Molecular Dynamics (MD) simulations and adopt the Berendsen thermostat. All the runs are performed in a simulation box of volume V with N_R and N_G particles, of species R and G respectively. The total number $N_{tot} = N_R + N_G$ of particles ranges from $N_{tot} = 10^4$ to $N_{tot} = 3 \times 10^4$. Periodic boundary conditions are used. Apart from the total volume fraction $\phi_{tot} = \frac{\pi}{6} N_{tot}/V$, the 2CM are further characterised by the composition parameter $c = N_R/N_{tot}$. We perform simulations for several 2CM at different compositions c and volume fractions ϕ_{tot}, as well as for several 1CM. Initial configurations are obtained by placing the particles at random in the simulation box and equilibrating them at high temperature $T = 100$. In this regime the attractive part of the interaction is negligible and the system reduces to a one-component HS fluid. To obtain a gel, the systems are quickly quenched to low temperatures ($T = 0.05$) so that the particle velocities are relaxed faster than the configurational degrees of freedom.[19] For every set of the chosen parameters c and ϕ_{tot} we simulated 10 independent realisations to improve the statistical relevance of the observed quantities. In the last part of the paper, we will also consider a model based on a continuous potential.

2.2. Phase diagram

Prior to engaging in the discussion about gelation kinetics, we briefly discuss some morphological features of arrested 2CM.

In Fig. 1 we analyse the results of percolation probability. An algorithm is used to identify the clusters. A particle is assumed to belong to the same cluster if its minimal distance r from any other particle of the cluster is $r \le \delta D$. Percolation is assumed in the presence of a cluster that continuously spans the simulation box and reconnects to itself along all the 3 axes. This condition is tested on up to 10 runs and the system is considered as percolating if it occurs at least in 50% of the runs (made on $N_{tot} = 10^4$ particles). The symbols in the left panel of Fig. 1 indicate for which composition and total volume fraction the simulated 2-component system does (coloured symbols) or does not percolate (open squares). Furthermore, we distinguish the single percolation, when only one of the components percolates (red circles), or whether dual percolation takes place (blue diamonds). By swapping the R and G labels, the underlying physics does not change, hence we construct the percolation probability diagram by varying the concentration between $c = 0.0$ (one-component system) and $c = 0.5$ (symmetric composition). At low volume fraction, particles do not percolate. This is similar to what is observed for the 1CM

system, in simulations with similar system size and attraction strength.[19] Above $\phi_{tot} = 0.1$, however, percolation is always observed for at least one species. As observed before, a region of double percolation develops at around $c = 0.5$, and widens upon increasing ϕ_{tot}. In this symmetric case, the two species form two intertwined but physically separated gel-like clusters: a bigel. In regions where only single-species percolation occurs, isolated clusters are made of one component form, which remain embedded in the percolating network provided by the other component. Because of the finite size of the simulated systems, the evaluation of the percolation probability is affected for the volume fractions lower than the 5%.

Together with the percolation diagram, in the right-hand side panel of Fig. 1, we present some snapshots of 2CM systems at different ϕ_{tot} and c (with $N_{tot} = 3 \times 10^4$ particles). The simulated (c, ϕ_{tot}) correspond to the values discussed later for the experiments. The different morphologies can be observed moving from a low R content ($c = 0.125$) to an equal composition ($c = 0.5$). Also the different global porosity is clearly visible, as for smaller densities the void fraction increases. This feature will be compared later with the experiments.

In the following sections, we report a study of the 2CM dynamics that helps to highlight the spinodal decomposition mechanism involved in the formation of what we called a bigel. We also provide a kinetic characterisation for the aggregation phenomena in the presence of more than one species.

2.3. Kinetics of bigel formation

We focus on the kinetics of bigels to answer the question of whether the *arrested demixing* process,[1] leading to bigel formation, can be considered as an arrested spinodal decomposition, similar to the case of 1CM gels.[13,19,27] For this purpose, several independent runs for both the 1CM and the 2CM are prepared with the same quenching protocol. In this section we focus on the structural evolution of the simulated systems, followed until the arrested state is reached, *i.e.* until the mean squared displacement (MSD) and the clustering have reached a plateau, and the potential energy undergoes only slight changes in time. We discuss further such quantities in what follows.

In Fig. 2a, we present the evolution of the MSD as a function of time, measured after the arrested state is reached. The particles start to collide after a characteristic time that, not surprisingly, shortens at increasing volume fraction. After this transient time, the MSD plateaus as a consequence of the arrest of the dynamics. The height of the plateau reflects a typical localisation length related to the space explored by particles within the arrested structure, once this is irreversibly formed. For the sake of comparison, we plot the results of one of the two sub-networks of a bigel along with the network of the corresponding 1CM gel at the same volume fraction, *i.e.* half the total bigel's volume fraction. The MSD shows similar trends for bigels at total volume fractions ϕ_{tot}, *i.e.* symmetric 2CMs with $c = 0.5$, and for gels (1CMs) at half the volume fraction. Because of the inherent symmetry of the 2CM, the distinct curves of its different components can be averaged among each other. The MSD results for single gels and for bigels (Fig. 1a) behave very similarly at low volume fraction, since the plateau of the MSD is reached roughly at the same time and has the same height. This suggests a similar localisation length. At high density, while the plateau is reached on similar timescales for both kinds of gels, its height is different. It appears that particles are more localised within the bigels than within the gels. This is an important difference between the two systems that is mainly due to steric

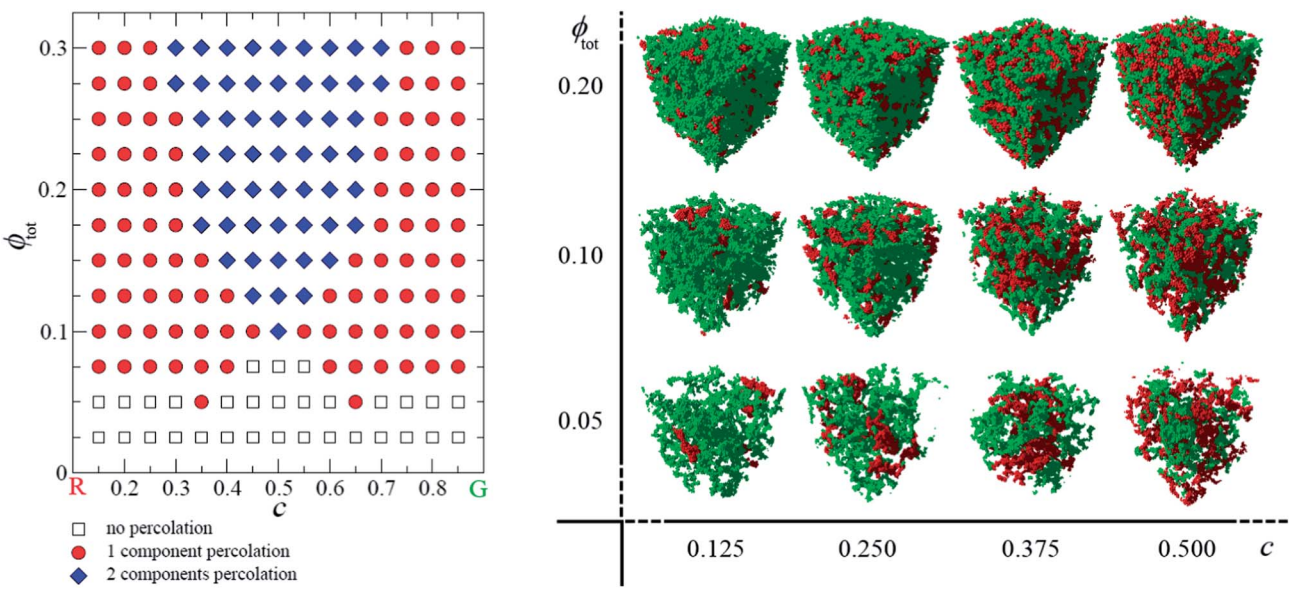

Fig. 1 (Left) The percolation occurrence is shown in the (c, ϕ_{tot}) diagram, where different symbols refer to a different percolation properties (see the legend). We observe lack of percolation for low volume fractions due to the finite size used for simulations ($N_{tot} = 10^4$). For asymmetric compositions c the percolation is dominated either by the red or by the green component, and the $c = 0.5$ symmetry emerges due to construction. (Right) A visual representation of the (c, ϕ_{tot}) diagram with snapshots of the arrested phases. As the same number of particles have been used at different ϕ_{tot}, boxes of different sizes have been used, but for simplicity they are scaled to the same size in the figure.

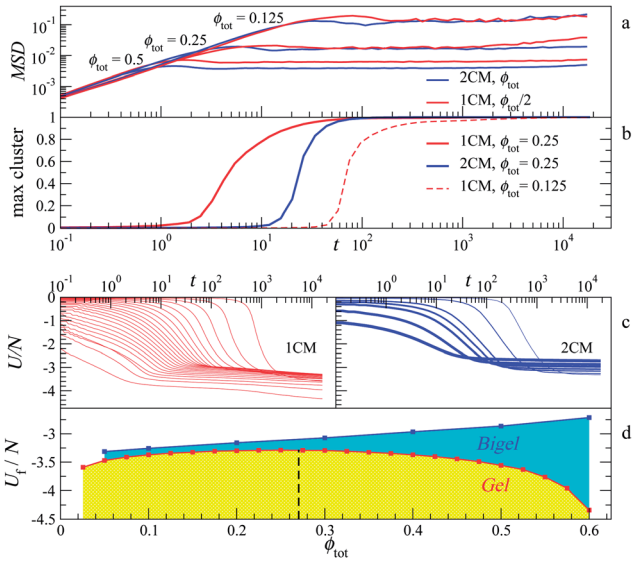

Fig. 2 (a) Plot of the *MSD* calculated for reference configurations after the structural arrest is reached. Along with the 2CM systems at ϕ_{tot}, we show the 1CM at half the volume fractions. The characteristic time needed for the *MSD* to reach a plateau decreases at increasing values of volume fraction. (b) The size of the largest cluster is normalised over the N_{tot} particles of the corresponding component. For clarity, here the comparison is limited to two 1CM and one 2CM. The characteristic aggregation time for a 1CM gel is larger if compared to the one relative to a 2CM at double the volume fraction, *i.e.* when the different species separately equal the volume fraction of the 1CM. When equal volume fractions are considered, gels aggregate faster than the bigels. (c) The dynamic arrest also is demonstrated by the evolution of the potential energy per particle U/N. The different curves are relative to the different volume fractions, whose values are plotted as square symbols in the last panel (ϕ_{tot} grows from right to left). (d) The final energy values U_f/N are shown as a function of the total volume fraction, both for gels (red) and bigels (blue). A slight drift in energy is still present, due to sporadic local rearrangements, and we plot the $U_f(\phi_{tot})$ values at the same run-time $t_f = 1.8 \times 10^4$.

effects. The two sub-networks of the bigels occupy space, and this encumbrance becomes more relevant as density is increased. This steric effect constrains the particles forming a bigel on smaller length-scales compared to the ones of the gels, an observation that will have important consequences on the mechanical properties of the bigels, as we will see later.

An alternative way of identifying timescales during the quench consists in characterizing the evolution of the colloidal clustering. In bigels, the clusters are defined by identifying the groups of bonded particles belonging to the same species. Only the particles belonging to the same species can form energetic bonds, therefore we consider only the clustering of one of the two species and we compare it to the 1CM's counterparts. In Fig. 2b we show the time dependence of the normalised size of the largest cluster, where the normalisation is made by dividing the size of the largest cluster over N_{tot} in the 1CM case, and over $N_{tot}/2$ in the 2CM case. For simplicity, here we compare a bigel ($\phi_{tot} = 0.25$, $c = 0.5$) with the gel having the same total volume fraction ($\phi_{tot} = 0.25$) and with another gel at half its volume fraction ($\phi_{tot} = 0.125$). By this comparison, we observe characteristic aggregation times that differ by at least one order of magnitude. More specifically, when the same total volume fraction is considered, 1CM aggregates faster than 2CM. This is a consequence of the fact that in 1CM, attractive particles encounter each other more frequently than in the 2CM case. On the other hand, when half of the volume fraction is considered, the aggregation of the bigels occurs more rapidly.

This behaviour, probably due to steric reasons, is robustly observed for all the tested volume fractions and highlights the major role played by the presence of a second species: the competition among the two species of a 2CM leads to differences between the characteristic clustering times, even at low densities. Namely, although the final arrested structures share the same topology,[1] at equal volume fraction of the single species of the 2CM and of the 1CM, the aggregation results faster in 2CM systems. When the total volume fraction is considered in both the systems, instead, the 1CMs result faster. In addition, we notice a different increase in the clustering curves, where the 1CM systems systematically present a more stretched shape by comparison to the curves referring to the bigel formation. This effect could reflect a different complexity in the two kinds of systems.

Apart from time-scales, other differences arise in the dynamics of quenched 2CM and 1CM. In Fig. 2c, we present the evolution of the energy during the quench for gels and bigels at different volume fractions. In square-well systems, the potential energy U is directly related to the number of bonds by the relation $n_B = -2U/N$. The energy decays after an initial plateau at a time that decreases upon increasing volume fraction, indicating the onset of aggregation. After such a decay, the decrease in energy slows down dramatically. It must be stressed that, while the dynamics is extremely delayed, the energy is still slightly evolving. This aging behaviour has been recently related to the fact that the temperature remains finite.[34] For the purpose of the present paper, we call this extremely slow evolution an arrested state; this is justified by the fact that, within our simulation time windows, we do not observe any radical structural rearrangement.

The final energies U_f depend on the volume fraction and, in agreement with what was observed before, the corresponding final n_B values depend non-monotonically on the volume fraction for 1CM gels.[15] In particular, as shown in Fig. 2d, at a volume fraction close to the critical value known for the adhesive hard-sphere model,[35,36] $\phi_c \approx 0.27$, a maximum of the $U_f(\phi)$ is found. This corresponds to a minimum in the $n_B(\phi)$ values for the arrested state. However this observation does not hold for the bigels, as the potential energy depends monotonically on the density of the system. It has been shown[37,38] that the liquid–vapor (LV) critical point becomes metastable with respect to the mixed–demixed fluid transition. This occurs as soon as the interspecies interactions are slightly reduced. We argue that this implies, for the strong non-affinity between the two species investigated here, that the LV critical point is well hidden below the demixing region and that, as a consequence, the density fluctuations associated with it are less pronounced.

2.4. Spinodal decomposition

In order to describe the kinetics of the formation of the bigels, it is important to define a characteristic domain size $L(t)$ that

grows with time during the separation. To do so, we use the evolution of the structure factor $S(k, t)$, an observable of central importance in the study of gelation phenomena.[10,39]

Following Thakre *et al.*[40] we define the structure factors for the two components as

$$S(k, t) = \langle \rho_k \rho_{-k} \rangle, \quad (2)$$

where ρ_k is the modified Fourier transform of the density variable.

$$\rho_k = \sum_{i=0}^{N_{tot}} b_i \exp(ik \cdot r_i(t)). \quad (3)$$

In the case of two components, b_i takes the values ± 1 depending on the component considered. This definition has been proved to be particularly suitable for the description of the kinetics during demixing.[40]

An analytical approximation for the resulting structure factor has been proposed by Furukawa[25]

$$S(k, t) = S_{max}(t) \frac{3(k/k_{max}(t))^2}{2 + (k/k_{max}(t))^6}, \quad (4)$$

where the parameter $S_{max}(t)$ refers to the maximum height of the structure factor at the wavenumber $k_{max}(t)$ of the small-k peak. The latter grows and shifts during gelation. Although eqn (4) is known to work only in dilute conditions, it can be used to extract information about the domain size and its changes in time, through the evolution of the fitting parameters. In fact, a fit made by using eqn (4) can be used to rescale the data and extract the domain size by using the relationship $L(t) = 2\pi/k_{max}(t)$.[40,41]

In Fig. 3a, we show the fits obtained at different times during the aggregation of a bigel with $\phi_{tot} \approx 0.125$. The relative curves are consequently collapsed on a master curve presented in Fig. 3b, where $x = k/k_{max}$ and $\bar{S}(x) = S(k,t)/S_{max}(t)$. The Furukawa scaling is associated with the late stages of the phenomenon of spinodal decomposition in polymeric and fluid mixtures.[42,43] Its unequivocal occurrence, in our case, reinforces the idea that spinodal decomposition is indeed the underlying physical phenomenon for the gelation of the multi-component colloidal system. The behaviour of both the $S_{max}(t)$ (not shown here) and $L(t)$ (in Fig. 3c for three different total densities) reflects the dynamical slowing down and successive structural arrest. In particular, for t sufficiently large such that the arrest has occurred, L identifies the characteristic distance between the ramified structures that form the bigel. Such a distance is sensibly shorter for higher densities, as a result of the decreased free volume, a behaviour that is directly reflected by the porosity.

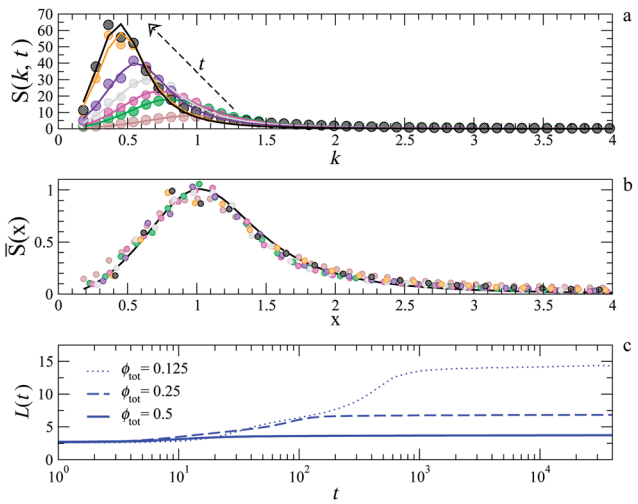

Fig. 3 (a) The analytical fitting provided by the Furukawa approximation is applied here to structure factor data $S(k)$ of a forming bigel with $\phi_{tot} = 0.125$, at different intermediate and late aggregation stages, from $t = 1.3 \times 10^2$ to $t = 6.9 \times 10^4$ in reduced time units. During the quench the $S(k, t)$ peak evolves and "freezes". (b) The Furukawa scaling makes it possible to collapse the $S(k, t)$ curves on a master curve: this represents a test for the occurrence of spinodal decomposition. The fitting allows the estimation of useful quantities for bigels. (c) Here we evaluate the characteristic length of the system, $L(t) = 2\pi/k_{max}(t)$, during the quench. Here we show it from the time when differences among the different volume fractions start being more relevant. The value k_{max} represents the k value relative to the peak evaluated at different times.

3. Experimental results

3.1. DNA-coated colloids

For the experimental investigation of the arrested demixing process we use DNA-coated colloids (DNACCs). Micrometre size DNA-coated particles functionalised with complementary single-stranded DNA (ssDNA) sequences are excellent gel-forming systems due to the strength and the sharp, reversible, thermal activation of hybridisation mediated interactions.[1,26,44–46] Such features are ascribable to the cooperativity between the many DNA strands involved in the interactions.[44,47–51]

Let us consider a solution containing equal concentrations of the ssDNA sequence A and its complementary A′. At high temperature most of the strands are in their monomeric state, *i.e.* the fraction of non-hybridised strands is $f(T) \approx 1$. At low temperature most of the A–A′ pairs are hybridised, *i.e.* $f(T) \approx 0$. For free strands in solution, the melting temperature T_m^{free} is defined as the temperature at which $f = 1/2$ and depends on the hybridisation free energy and the DNA concentration. The width of the hybridisation transition, approximated by $\left[\frac{\partial f}{\partial T}\right]^{-1}_{f=1/2}$, can be as large as 10–20 °C.[52]

Analogously, we can consider a binary mixture of colloids containing particles A and A′ functionalised with the corresponding strands. At high temperatures, the DNA brushes covering the particles only produce a steric repulsion. By lowering the temperature, hybridisation interactions induce a strong attraction between particles A and A′. Similar to the case of free DNA, we can define a melting temperature T_m as the temperature at which 1/2 of the particles are in the monomeric state. Due to the large number of ssDNA strands involved in the interaction between each pair of particles, the width of the

melting/aggregation transition in DNACCs is much narrower than the one measured for free ssDNA strands, typically ~1 °C.[44,47,48] By crossing this sharp transition, we can turn the DNACC interactions from purely repulsive to strongly attractive with an interaction energy $\lesssim -10k_BT$. This feature allows an almost instantaneous activation of attractive interactions, which well approximates the instantaneous quenches performed in simulations.

Contrarily to more traditional means of inducing attractive colloidal interactions, such as the addition of depletant polymers,[13,14] DNA-mediated interactions are selective. This property allows one to design binary mixtures in which, as required for bigels, only intra-species (R–R and G–G) attraction is present, whereas inter-species interactions (R–G) remain repulsive regardless of the temperature.[1,26] The coating design adopted to reproduce this interaction scheme is sketched in Fig. 4. The two species of colloids, R and G, are functionalised with a symmetric mixture of ssDNA strands: A and A′ for colloids G and B and B′ for colloids R. These *sticky ends* are not grafted directly to the surface but tethered *via* an inert double-stranded DNA (dsDNA) spacer with a length of $L \sim 20$ nm (60 base pairs). The spacers allow the sticky ends to explore a larger volume around their grafting point and reduce the entropic cost for hybridisation between two tethered strands. The persistence length of dsDNA is ~40 nm, therefore the inert spacers can be regarded as rigid rods. To enhance the pivoting motion of the DNA constructs we introduce flexible 5-thymine spacers between the grafting point and the dsDNA and between the dsDNA and the sticky end.

The interspecies G–G and R–R attraction is guaranteed by the formation of inter-colloidal *bridges* following from the hybridisation of complementary strands grafted to the surface of approaching colloids. Even if some of the tethers form *loops* due to the hybridisation of complementary strands grafted on the same colloid, the number of bridges is enough to guarantee a strong attraction between particles below the melting temperature.[49–51]

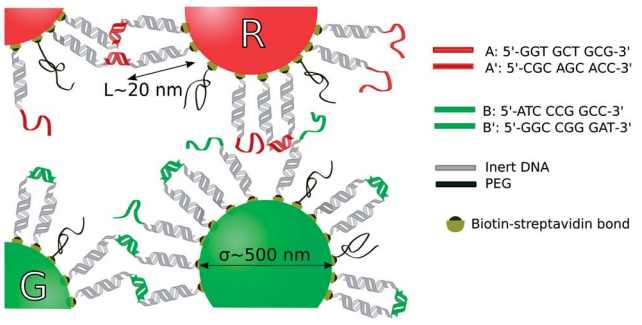

Fig. 4 Not to scale diagram showing the surface functionalisation of our binary colloidal mixtures. G and R particles are coated with DNA constructs made of a dsDNA spacer (grey double helices) and an active sticky end (red strands for A and A′, green strands for B and B′). The constructs are grafted to the colloids *via* biotin–streptavidin bonds. For $T < T_m$, A–A′ and B–B′ bridges form between neighboring R and G colloids respectively, giving rise to an attractive intra-species interaction. PEG polymers (black strands) are introduced to reduce the overall density of the DNA coating and tune the melting temperature.

The A–A′ and B–B′ sequences, shown in Fig. 4, are designed to have a very similar T_m^{free} (37.5 °C and 37.8 °C for A–A′ and B–B′ for a concentration of 0.25 μm with 50 mM ionic strength). This results in single T_m for R and G colloids, below which the intra-species attraction is activated for both species. The binding probability between A (A′) and B (B′) strands is always negligible in experimentally accessible conditions, resulting in a repulsive inter-species interaction.

While other sources of interaction (electrostatic repulsion, dispersion attraction, *etc.*) are negligible, the range of the DNA mediated attraction is ~L, about 4% of the colloidal diameter $\sigma \approx 500$ nm. Noro and Frenkel demonstrated that for sticky spheres with an attraction range <5% of the particle diameter, the thermodynamics is only influenced by the second virial coefficient, independent of the functional form of the potential.[32,35,53] This observation justifies the choice of the numerical models we use in our simulations.

3.2. Sample preparation

As shown in Fig. 4, we coat our particles with four DNA constructs of the sequence

biotin-5′-TTTTT-dsDNA spacer-TTTTT-sticky end-3′,

where the sticky end is either A, A′, B or B′.

The rigid dsDNA spacer is assembled before grafting the constructs to the colloids by hybridising the ssDNA strands:

(i) Biotin-5′-TTTTT-S-TTTTT-sticky end-3′

(ii) S′where the ssDNA S and S′ are complementary to each other:

S: 5′-GAG GAG GAA AGA GAG AAA GAA GGA GAG GAG AAG GGA GAA AAG AGA GAG GGA AAG AGG GAA-3′

S′: 5′-TTC CCT CTT TCC CTC TCT CTT TTC TCC CTT CTC CTC TCC TTC TTT CTC TCT TTC CTC CTC-3′.

Strands (i) and (ii) (Integrated DNA Technology) are dissolved in Tris–EDTA buffer (TE, Sigma Aldrich) in a 1 : 2 concentration ratio, then heated up to 80 °C for 2 hours and allowed to slowly cool down to room temperature for more than 6 hours to allow the hybridisation of S and S′. For simplicity we refer to the whole DNA constructs with the label of their sticky ends.

For all the experiments reported here, we use polystyrene (PS) particles with $\sigma \approx 500$ nm (Microparticles GmbH, Berlin). To make them distinguishable in confocal microscopy and epifluorescence experiments we use green fluorescent (FluoGreen 492/519 nm) and red fluorescent (FluoRed 530/607 nm) particles. The particles are coated with streptavidin in order to graft the biotin-labeled DNA to them.

Before carrying out the grafting protocol, the particles are sonicated for 15 minutes in order to break nonspecific aggregates. The colloids are then suspended in a solution containing A and A′ constructs for R particles and B and B′ constructs for G′ particles. The A : A′ and B : B′ ratios are kept to 1 : 1 and the

overall DNA concentration is tuned to guarantee at least a 10× excess compared to the overall binding capacity of the colloids in solution.

To allow for dense grafting, the colloids/DNA solutions are kept at room temperature for at least 2 hours. The addition of NaCl, up to 500 mM, is found to improve the coating density.

A fraction of inert polyethylene-glycol chains (5 kDa biotin-PEG, Laysan Bio Inc., Arab, USA), in 0.3× excess, is added to the coating solution in order to reduce the DNA grafting density, and thereby the melting temperature of the colloids. Since the radius of gyration of the polymer is much smaller than the length of the DNA strands, the PEG does not influence the steric repulsion.

After the incubation, the colloidal solutions are pelleted by centrifuging at 12 100× g for 5 minutes, the supernatants are removed, the particles resuspended in fresh TE buffer and kept at 45 °C for ∼3 minutes. This washing cycle is repeated 5–10 times in order to get rid of all the unbound DNA. Afterwards, the particles are pelleted and resuspended in an appropriate volume of TE buffer with the addition of 50 mM NaCl and sucrose in order to match the density of PS particles, *i.e.* $\rho = 1.05$ g cm^{-3}.

The colloids have a measured binding capacity of $\sim 2 \times 10^4$ strands per particle, in agreement with the nominal value provided by the manufacturer. To measure the binding capacity, we carry out a coating protocol with a known amount of particles and a small ($\approx 2\times$) excess of DNA. The binding capacity is determined by measuring the fraction of unbound DNA remaining in solution after the incubation.

Due to the high refractive index of PS and the incompatibility of DNA with organic solvents, it is impossible to achieve refractive-index matching of our solutions. In order to guarantee good optical imaging of otherwise opaque colloidal samples we build glass sample chambers in a slab (quasi-2D) geometry with an almost uniform thickness of 10–15 μm in the z direction and surface area of 18 × 18 mm in the x–y plane.[26] Once filled with 6–8 μl of sample solution, the chambers are immediately sealed with a two component epoxy glue to prevent any evaporation.[26]

Before constructing the chambers, we wash the glass components (microscope slides and coverslips) in strong surfactant solution (1% Hellmanex, Hellma Analytics) at high temperature, sonicate them to desorb any impurities and rinse in double-distilled water. To improve hydrophilicity the glass is soaked for 5 minutes in 3 M NaOH solution, then rinsed again. Immediately before filling them, we process the sample chambers for 30 seconds in a plasma-cleaning machine (Diener Electronic Femto). These treatments prevent the colloidal particles from sticking to the surfaces of the chambers, which act as almost ideal hard walls.

The two colloidal components G and R are mixed before being injected in the chamber. At this stage we add 1 μl of a 0.2 mM solution of biotin (≥99% powder, Sigma-Aldrich) dissolved in density matched TE buffer. The biotin saturates all the available binding sites on the surface of the colloids and prevents eventually free DNA from grafting on the surface of colloids of the wrong species, which would produce undesired inter-species attraction.

Both the colloidal solution and the sample chamber are heated up to 60 °C before injection in order to break DNA-mediated colloidal aggregates.

Once sealed, the samples are transferred on a Nikon Eclipse Ti-E inverted microscope equipped with a PLAN-APO 20/0.75 dry objective and a Ximea MQ013MG-E2 camera (E2V EV76C560 CMOS sensor). The samples are heated up to $T_{\mathrm{in}} = 55$ °C, above the melting temperature T_{m}, using a copper heating block that ensures a uniform temperature across the chamber. Finally, the samples are allowed to equilibrate at T_{in} until a uniform gas phase is formed, then the temperature is gradually reduced until gelation occurs.

3.3. Imaging and image analysis

The evolution of the samples from the high temperature gas phase to the low temperature arrested structures is monitored by taking epifluorescence snapshots $E_{\mathrm{R/G}}(x, y, t)$ at intervals of 15 s, alternating R and G channels. From the Fourier-transformed images $E_{\mathrm{R/G}}(k_x, k_y, t)$ we calculate the structure factor $S_{\mathrm{R/G}}(k, t) = I_{\mathrm{R/G}}(k, t)/|f_{\mathrm{R/G}}(k)|^2$, where $f_{\mathrm{R/G}}(k)$ is the form factor and

$$I_{\mathrm{R/G}}(k,t) = \frac{\left\langle \left| E_{\mathrm{R/G}}(k_x, k_y, t) \right|^2 \right\rangle}{\sum_x \sum_y E_{\mathrm{R/G}}(x,y,t)}. \quad (5)$$

In the above equation $\langle \ldots \rangle$ indicates a radial average carried out on a single image, $k = \sqrt{{k_x}^2 + {k_y}^2}$ is the wave vector and the sum is extended to all the pixels of the image. An approximation for $|f_{\mathrm{R/G}}(k)|^2$ is given by $I^{\mathrm{gas}}_{\mathrm{R/G}}(k, t)$, measured for the colloids at $T > T_{\mathrm{m}}$, which allows us to finally obtain the structure factor as

$$S_{\mathrm{R/G}}(k,t) \approx \frac{I_{\mathrm{R/G}}(k,t)}{\left\langle I^{\mathrm{gas}}_{\mathrm{R/G}}(k,t) \right\rangle_{t, T=T_{\mathrm{in}}}}, \quad (6)$$

where $\langle \ldots \rangle_{t,T=T\mathrm{in}}$ indicates a time average at constant temperature.

At the onset of gelation, $S_{\mathrm{R/G}}(k, t)$ develops a peak that narrows and migrates towards lower values of k, stabilizing when kinetic arrest occurs.[13,14] To track the phase separation process we measure the two observables: the peak height $\mathrm{M}(t) = \max[S_{\mathrm{R/G}}(k, t)]$ and the first moment $k_1(t) = \sum_{k=0}^{\tilde{k}} k S_{\mathrm{R/G}}(k,t) \Big/ \sum_{k=0}^{\tilde{k}} S_{\mathrm{R/G}}(k,t)$, where $\tilde{k} = 4.6$ μm^{-1}.[15]

It should be noted that, given the slab geometry of the chambers, epifluorescence snapshots integrate information from the whole thickness of the sample. However, since the gel branches do not appear to overlap with each other along the z (axial) direction, the structure factors extracted from these projected images are expected to faithfully capture the morphological features of the aggregates at small and intermediate wave vectors.

Once cooled down to room temperature, the arrested structures are imaged on a confocal microscope for structural characterisation. We used either a Leica TCS SP5 microscope equipped with a HCX PL APO CS 100/1.4 oil immersion or a Zeiss LSM 510 microscope with a FLUOTAR 100/1.32 (Leitz

Wetzlar, Germany) OEL ICT oil immersion objective. Confocal stacks are taken over a volume of $\approx 150 \times 150 \times 20\ \mu m^3$, which covers the whole thickness of the slab-geometry chambers. The morphology of the bigels is characterised by the chord-distribution analysis of single confocal images taken from the middle of confocal stacks.

Confocal images from both G and R channels, $J_R(x, y)$ and $J_G(x, y)$, with $J_{R/G}(x, y) \in [0, 255]$, are smoothed with a Gaussian filter and thresholded in order to produce binary images $J^T_{R/G}(x, y)$. Given an integer threshold $\Gamma \in [0, 255]$, the binarised images are given by

$$J^T_{R/G}(x,y) = \begin{cases} 0 & \text{if } J_{R/G}(x,y) < \Gamma \\ 1 & \text{if } J_{R/G}(x,y) \geq \Gamma \end{cases}. \quad (7)$$

To guarantee unbiased results when comparing images from different samples, we define an algorithm to set the value of the threshold Γ for each image. For all the $\Gamma_n = 1 \ldots 255$, we can calculate the normalised overlap between R and G domains:

$$\Omega_n = \frac{\sum_x \sum_y J^T_{R,n}(x,y) \wedge J^T_{G,n}(x,y)}{\sum_x \sum_y J^T_{R,n}(x,y) \vee J^T_{G,n}(x,y)}, \quad (8)$$

where $J^T_{R/G,n}(x, y)$ are the binarised images calculated according to the threshold Γ_n. For small Γ_n, G and R domains will display a significant overlap, corresponding to a large Ω_n. The overlap will decrease monotonically as we increase Γ_n. After setting a tolerance $\varepsilon = 0.02$, we take the threshold Γ equal to the smallest Γ_n for which $\Omega_n \leq \varepsilon$, and calculate $J^T_{R/G}(x,y)$ accordingly.

Chord distributions[1,16,22,23,26] are calculated by drawing straight lines on the thresholded images and measuring the length r of the intersections between such lines and the R/G domains, the overall gel network identified by $J^T_{tot}(x,y) = [J^T_R(x,y) \vee J^T_G(x,y)]$, and the pore network identified by $J^T_p = 1 - J^T_{tot}$. Since the bigel structures are isotropic, the straight lines are traced on a regular grid along the x and y directions. For each sample, $f(r)$ is sampled on 15–25 independent images.

The probability distribution $f(r)$ of the chord-lengths, for R and G, the overall gel, and for pores, exhibits an exponentially decaying tail, which we fit with the function $f(r) = f(0)\ \exp(-r/\lambda)$. The decay length λ is a measure of the persistence length of the structures,[22,23] and is proportional to the typical length-scale of the kinetic arrest,[16] $L(t \to \infty)$. Fractal structures, which have no intrinsic length-scale would produce chord-distributions with a power-law decay, the exponent of which is related to the fractal dimension.

We introduce a further parameter to gather information on the morphology of our aggregates. From R and G binarised images we measure a non-dimensional contour-to-area ratio:

$$\Pi_{R/G} = \frac{\lambda_{R/G} \sum_x \sum_y C^T_{R/G}(x,y)}{\sum_x \sum_y J^T_{R/G}(x,y)}, \quad (9)$$

where

$$C^T_{R/G}(x,y) = \begin{cases} 1 & \text{if } J^T_{R/G}(x,y) = 1 \wedge J^T_{R/G}(x \pm 1,\ y \pm 1) = 0 \\ 0 & \text{otherwise} \end{cases} \quad (10)$$

is the binarised image tracing the contour of $J^T_{R/G}(x, y)$. With the factor $\lambda_{R/G}$ in eqn (9), we rescale the contour-to-area ratio by the typical length-scale of the aggregates. This is necessary given that samples with the same morphology have a smaller contour-to-area ratio if the structures are larger.

With the parameter Π, we determine how *elongated* the bigel structures are. A high value of Π indicates a predominance of elongated structures, while low values suggest more compact structures with sphere-like clusters.

3.4. Experimental phase diagram

We characterise the morphology of arrested bigels as a function of the total volume fraction ϕ_{tot} and the R–G composition c. In Fig. 5 we show four confocal images with the relative binarised versions for samples with $\phi_{tot} \approx 0.10$ and variable c. The four samples have nominal c values equal to 0.5, 0.375, 0.25 and 0.125. For the same samples we can estimate c from thresholded confocal images as

$$c \approx \left\langle \frac{\sum_x \sum_y J^T_R(x,y)}{\sum_x \sum_y J^T_R(x,y) \vee J^T_G(x,y)} \right\rangle, \quad (11)$$

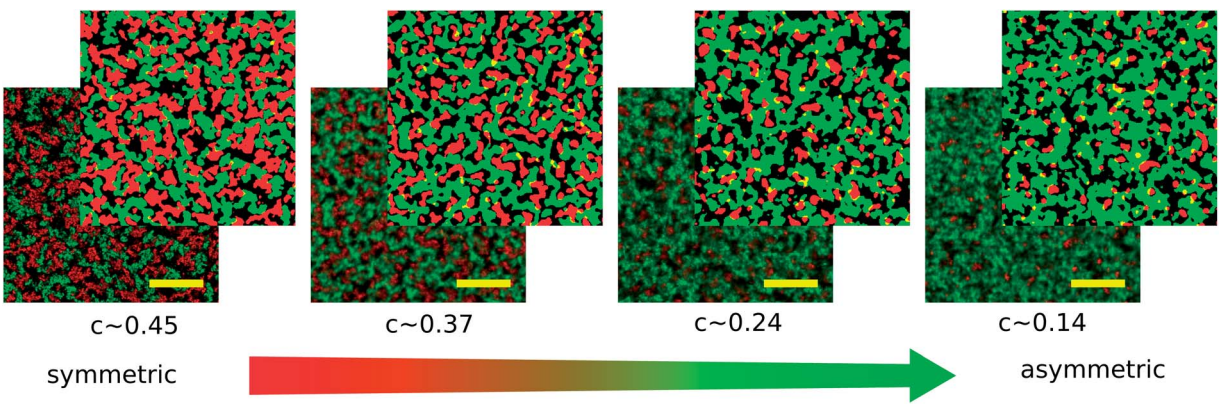

Fig. 5 Confocal microscopy and relative binarised images for arrested bigels with $\phi_{tot} \approx 0.10$ and variable c. The reported values of c are measured from binarised images according to eqn (11). The scale-bars are equal to 30 μm.

Eqn (11) gives $c = 0.45 \pm 0.03$, 0.37 ± 0.03, 0.24 ± 0.02 and 0.14 ± 0.01, in good agreement with the nominal values. The average indicated by $\langle \ldots \rangle$ has been performed, respectively, over 15, 25, 25, and 20 images. The errors indicate the standard deviation.

In the symmetric bigel with $c \approx 0.45$ both components show a branched inter-percolating structure, as expected from computer simulation results.[1] As mentioned above, in experiments performed in quasi 2D the gel branches belonging to different components are very unlikely to overlap with each other in the z direction. For this reason percolation over the whole size of the sample is hindered for both the components. By reducing c, the G phase becomes in excess compared to the R one, and the G branches percolate over larger distances. For the most asymmetric sample with $c \approx 0.14$, R colloids only form small clusters embedded within a percolating G network. These qualitative observations are supported by chord distribution analysis. In Fig. 6a, $f(r)$ measured for R and G components for the four samples shown in Fig. 5 is presented. In Fig. 6b we show the $f(r)$ of the overall gel and pores measured for the same samples. The fitted λ values are plotted as a function of c in Fig. 6c. At low c, we find $\lambda_G \gg \lambda_R$; by increasing c, λ_G decreases and λ_R increases monotonically until both the persistence lengths converge to ≈ 2.1 μm for $c \approx 0.45$. The persistence length λ_{tot}, calculated for the overall gel, and λ_p, calculated for the pore network, decrease monotonically upon increasing c.

The non-dimensional contour-to-area ratio $\Pi_{R/G}$ is plotted in Fig. 6d. For very asymmetric samples, we find that Π_G is about twice Π_R, confirming that the component in excess, G, tends to form more elongated structures, whereas the low-concentration component, R, forms more rounded clusters. By increasing c, Π_G decreases monotonically and Π_R increases monotonically.

For a direct comparison of the simulated and experimental morphology of the bigels we perform chord-distribution analysis and measure the Π values from simulation data. To do so, we produce "simulated" confocal images from the single-particle coordinates of bigels generated *via* molecular dynamics at various values of c. We consider a slice of the cubic simulation box with a thickness equal to twice the particle diameter and parallel to the x–y plane. Both R and G images are generated by projecting on the x–y plane all the R and G particles intersecting this slice [Fig. 6e (left)]. The images are then blurred with a Gaussian filter to mimic the experimental resolution [Fig. 6e (middle)], and binarised in order to extract the chord distribution function and the contour-to-surface ratio [Fig. 6e (right)]. For each simulation 20 equally spaced slices of the box are taken.

In Fig. 6f we show the c dependence of $\lambda_{R/G}$, λ_{tot}, and λ_p as extracted from computer simulations. For $\lambda_{R/G}$ and λ_{tot}, we notice a qualitatively similar trend compared to the experimental data in panel c. The simulated λ_p are comparatively larger than the experimental values. This difference is once again ascribable to the quasi-2D geometry of the experimental chambers that forces the gel branches to align along the x–y plane, where the chords are measured. This causes an apparent higher density and leads to an underestimation of the typical pore size. In simulations this effect is absent because the gel branches are randomly oriented with respect to the x–y plane. In Fig. 6g we plot the simulated $\Pi_{R/G}$; in this case the agreement between simulations and experiments is semi-quantitative

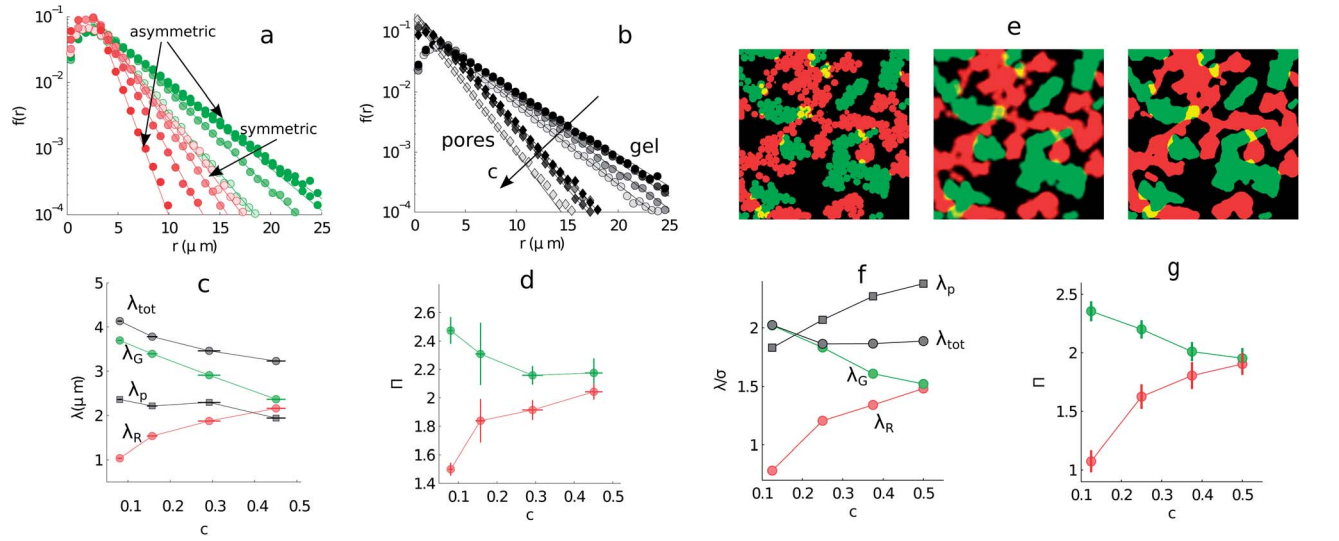

Fig. 6 (a) Chord-distribution $f(r)$ measured for the four samples in Fig. 5 ($\phi_{tot} \approx 0.10$ and $c = 0.45 \pm 0.03$, 0.37 ± 0.03, 0.24 ± 0.02 and 0.14 ± 0.01). Green and red circles (○) indicate G and R components respectively, where full symbols represent asymmetric compositions and empty symbols symmetric ones. Solid lines are exponential fits. (b) $f(r)$ measured for the same samples for the total gel (○) and the pore network (◇), again with full symbols representing asymmetric compositions and empty symbols the symmetric ones. Solid lines are exponential fits. (c) The persistence lengths λ_G, λ_R, λ_{tot} and λ_p fitted from panels a and b. (d) Non-dimensional contour-to-area ratios Π_R and Π_G measured for the same four samples. (e) Sequence of the three processing stages to obtain simulated confocal images from computer simulations. From left to right: image showing the intersection of G and R particles with a slab of height 2D; the same image blurred with a Gaussian filter; the same image thresholded with the Otsu's method (built-in Matlab function[54]). (f) $\lambda_{R/G}$, λ_{tot}, and λ_p from computer simulation data for a sample with $c = 0.5$ and $\phi_{tot} = 0.20$. (g) $\Pi_{R/G}$ from the same simulated sample.

demonstrating that the simulations correctly reproduce the shape of the arrested aggregates.

Besides the slab geometry of the sample chambers, another key difference between simulations and experiments contributes to explain the quantitative morphological mismatch. In experiments, the rolling movement of one particle against the other is expected to be kinetically hindered due to the large number of DNA strands mediating the attraction. On the other hand, in simulations, such a movement is free from kinetic hindrance. This may cause a higher packing of the particles within the simulated aggregates, compared to the experiments.

In Fig. 7a we show three confocal images with the binarised pictures for samples with $c \approx 0.5$ and $\phi_{tot} \approx 0.05, 0.10, 0.20$. The persistence lengths λ_G, λ_R and λ_{tot} exhibit only a slight change when increasing ϕ_{tot} from 0.05 to 0.10 but rise significantly when $\phi_{tot} = 0.20$. The increase is particularly evident for λ_{tot}. This is caused by the significant increment of the contact area between G and R domains following from the increase in volume fraction. As a result, many long chords spanning both G and R domains contribute to the chord distribution for the total gel, ultimately causing a larger λ_{tot}.

3.5. Experimental demixing dynamics

The arrested demixing process is experimentally demonstrated in Fig. 8. In panels a and b we show the time evolution of the structure factor maximum M(t) and the first moment $k_1(t)$, calculated separately for G and R components as described above. The data are relative to a sample with $\phi_{tot} = 0.10$ and $c \approx 0.5$ that is quenched well below T_m, heated up to $T_{in} = 55$ °C, and finally quenched again as demonstrated by the temperature profiles. The structure factor maximum sharply increases upon crossing the melting temperature, which for this sample is ≈ 50 °C, and plateaus as soon as kinetic arrest interrupts the spinodal decomposition. Analogously, the first moment drops when the demixing is triggered, and shortly saturates. Both observables reverse to their gas-phase values upon heating above T_m, and reproducibly follow the same trend when the second quench is performed. In Fig. 8c we present epifluorescence snapshots from the same experiment showing the two components in the gas phase before the first quench, in the bigel phase after the first quench, again in the gas phase after melting, and finally in the bigel phase following the final quench.

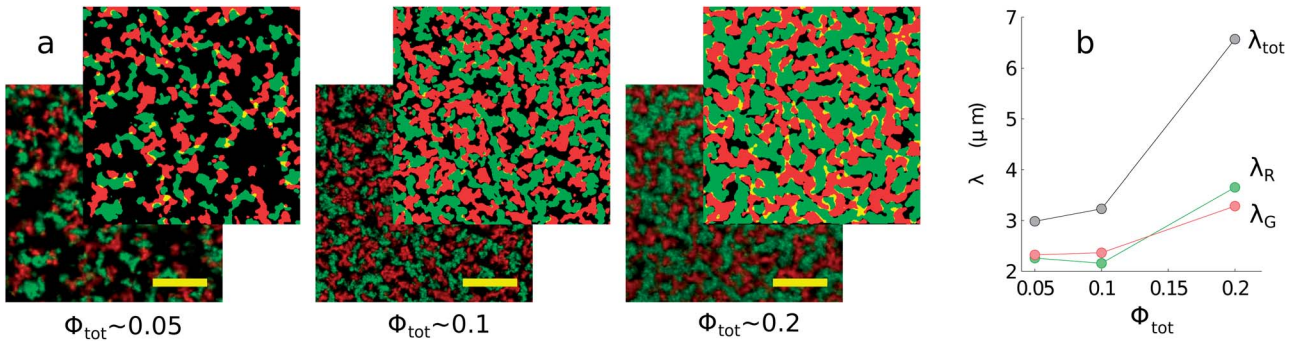

Fig. 7 (a) Confocal microscopy and corresponding binarised images for arrested bigels with (nominal) $c \approx 0.5$ and $\phi_{tot} \approx 0.05, 0.10, 0.20$. The scale-bars are equal to 30 μm. (b) Persistence lengths λ_G, λ_R, λ_{tot} measured from the samples shown in panel a.

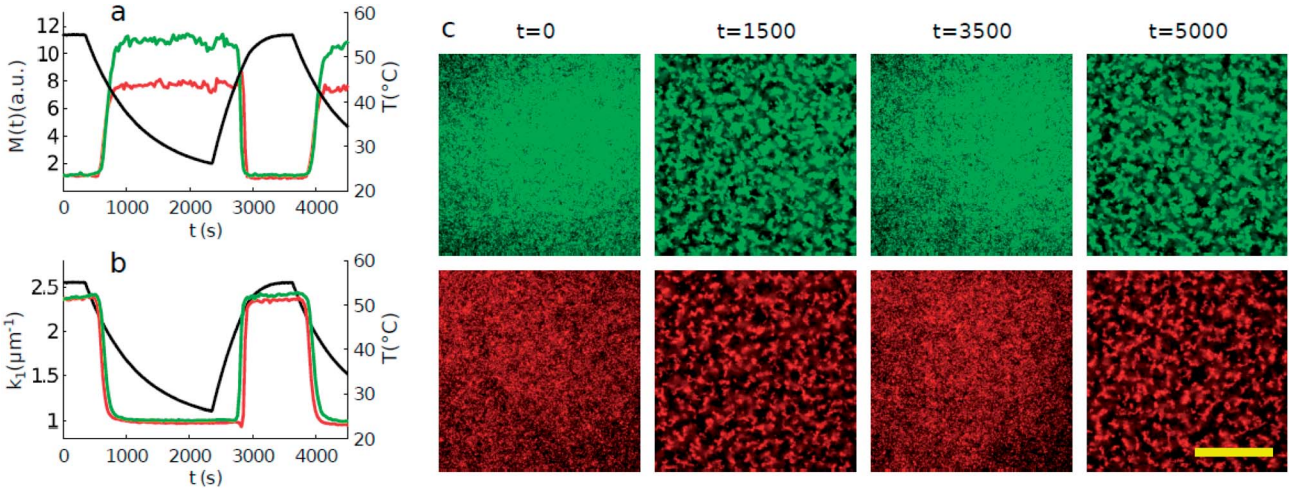

Fig. 8 Sample with symmetric composition and $\phi_{tot} \approx 0.10$ undergoing a double gelation–melting cycle. (a) Structure factor peak M(t) (left axis, red and green solid lines). (b) First moment $k_1(t)$ (left axis, red and green solid lines). In panels a and b black solid lines show the temperature (right axis). (c) Epifluorescence snapshots of R and G components. The scale bar equals to 40 μm.

The trends of M(t) and $k_1(t)$ qualitatively demonstrate the occurrence of arrested phase separation in experimental bigels. Nonetheless, an analysis of the Furukawa scaling analogous to that performed on computer simulations cannot be applied to the experimental data. The reason is that with the present experimental setup we can only acquire images of the G and the R components with a few seconds delay. A calculation of the overall experimental structure factor analogous to that described by eqn (2) and (3) would require epifluorescence snapshots taken (almost) simultaneously for both the components.

4. Mechanical properties of bigels

After having characterised the bigel formation and the resulting arrested structures, we now turn to the study of their mechanical properties. We investigate the bigels' behaviour under an externally imposed strain and compare it with that of gels. To do so, rather than using the square-well potential considered above, we simulate particles interacting *via* a modified version of the Lennard–Jones (MLJ) potential. Differently from the SW potential, the MLJ potential is continuous and allows the computation of derivatives, thus offering the possibility of carrying out conventional MD, rather than event-driven MD. In addition, the use of the MLJ potential allows us to verify that the bigel formation does not strictly require SW systems only, but that it is a more general phenomenon related to the short attractive interaction range. The modified LJ potential generalised to the case of 2CM can be written as

$$U_{\alpha\beta}(r) = \begin{cases} 4\varepsilon\left(\left(\frac{D}{r}\right)^{n} - \left(\frac{D}{r}\right)^{m}\right) + U_{\text{shift}}, & \text{if } r \le \delta_{\alpha\beta}D \\ 0, & \text{if } r > \delta_{\alpha\beta}D \end{cases}, \quad (12)$$

where we set the exponents as $n = 64$ and $m = 32$ so that the need for a sufficiently short-ranged potential is met. The attraction and repulsion are determined by the cut-off range: by setting $\delta_{RG} = 1$ and $\delta_{RR} = \delta_{GG} = 1.4$ the inter-species interaction is made purely repulsive, whereas attraction exists for particles of the same species. The choice of the other parameters is $\varepsilon = 1$ and $D = 1$, while U_{shift} is chosen to make the interspecies potential U_{RG} continuous at the cut-off distance $r = \delta_{\alpha\beta}D$. Being smooth, the MLJ is a somewhat more realistic description of a real colloid–colloid interaction potential.

For our simulations we use the open source MD simulation package LAMMPS,[55] which can deal with large systems and runs in parallel on multiple CPUs. Furthermore, LAMMPS supports energy minimisation techniques and offers the possibility to simulate mechanical deformations. The MLJ potential is not available in LAMMPS but was coded starting from the templates available in the LAMMPS package.

4.1. Gelation with the MLJ potential

By making use of the Berendsen thermostat in a simulation box with periodic boundary conditions, as for the previous SW simulations, after initially equilibrating at $T = 100$, the systems are quenched and finally allowed to evolve at $T = 0.01$. Given the low quench temperature, a short-ranged attraction prevails with a range close to the potential minimum $r_{\min} = \sqrt[32]{2} \approx 1.025$, *i.e.* close to the 3% used in the previous numerical model. Simulations of a 1CM and a symmetric ($c = 0.5$) 2CM containing a total $N_{\text{tot}} = 5 \times 10^4$ particles are performed, at volume fraction $\phi_{\text{tot}} = 0.10$. By using the same total volume fraction in both cases, we aim to highlight differences in behaviour ascribable to the presence of more components.

Visual inspection of the configurations obtained at the end of the quench confirms – for both 1CM and 2CM – the formation of gel-like structures. The analysis of the evolution for the potential energy, the MSD (not shown here) and the structure factor during the quench present the same features observed in the SW model. In particular, for the 2CM we show in Fig. 9a the $S(k)$ is expressed in eqn (2) and (3). The data of Fig. 9b follow approximately the Furukawa approximation of eqn (4), similar to what was already observed for the SW model. Therefore they can be collapsed on the same curve, thus suggesting the occurrence of spinodal decomposition. The observations of the dynamical arrest and of the approximate scaling of the structure factor do confirm that bigel formation is a general phenomenon, robust under a modification of the interaction potential, and thus it is not associated with the SW potential only.

4.2. Deformation with the AQS procedure

After the formation of the gel-like structures, we study the mechanical properties of the obtained samples. Quenched configurations that have reached a plateau in the potential energy and MSD are subjected to a potential energy minimisation using the conjugate-gradient method. This allows the systems to reach a mechanically stable minimum. Afterwards, such configurations are deformed (shear-strained) by varying the Lees–Edwards boundary conditions using the so-called Athermal Quasi-Static procedure (AQS).[56] This consists in iterating two steps: an initial configuration is deformed by affinely displacing the particles slightly (using a transformation of the

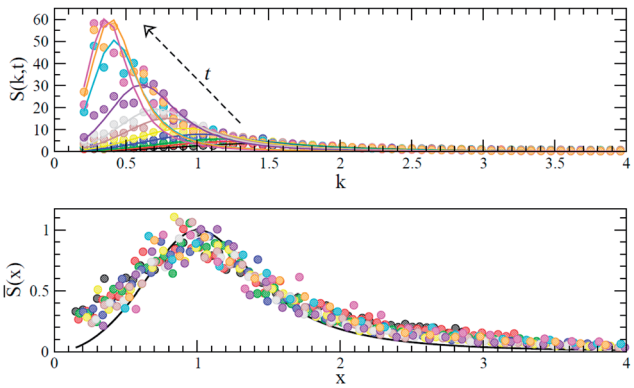

Fig. 9 (Top) Structure factor data during the quench for a single realisation of the symmetric 2CM ($c = 0.5$) at $\phi_{\text{tot}} = 0.1$ and $N_{\text{tot}} = 5 \times 10^4$. Data are collected at different intermediate and late aggregation stages, from $t = 2.21 \times 10^2$ to $t = 4.455 \times 10^3$ in reduced time units (bottom). Data can be rescaled so as to be collapsed onto the same curve. Here the collapse results are less effective than for the SW model.

form $x' = x, y' = y + x\mathrm{d}\gamma, z' = z$), thus incrementing the strain by a small amount $\mathrm{d}\gamma = 10^{-5}$. Afterwards, the potential energy of the deformed configuration is minimised according to updated boundary conditions consistent with the strain increment $\mathrm{d}\gamma$. By applying these two steps repeatedly, one can make the samples reach arbitrarily large shear strains. This protocol is suitable for studying systems at sufficiently low temperatures so that particles can be considered as "sticky", *i.e.* bonds between them only break because of changes in the strain on the system and not by thermal fluctuations. In AQS the temperature of the system is kept to zero by construction, thus all thermal effects are suppressed.

Values of the shear stress σ in the direction of the applied strain γ and the relative particle configurations are periodically stored, so that the evolution of the sample under deformation can be monitored. In Fig. 10 we plot the resulting stress *vs.* strain curves. The behaviour of 1CM and 2CM is strikingly different: first, the one-component gel appears to be softer than the bigel; second, the bigel has a higher yield stress (defined as the peak value of the stress *vs.* strain curve) than the gel; third, at large strain values, the bigel has a higher value of the stress than the gel. This last observation is related to the structural evolution of the ramified structures under deformation. As visible in Fig. 11, as strain is increased the 1CM system fractures and becomes more compact and particles lump into a single cluster. The 2CM, instead, breaks into several clusters composed of particles of different species that are in contact with each other, so that the structure does not become compact and remains a spatially homogeneous gas of clusters.

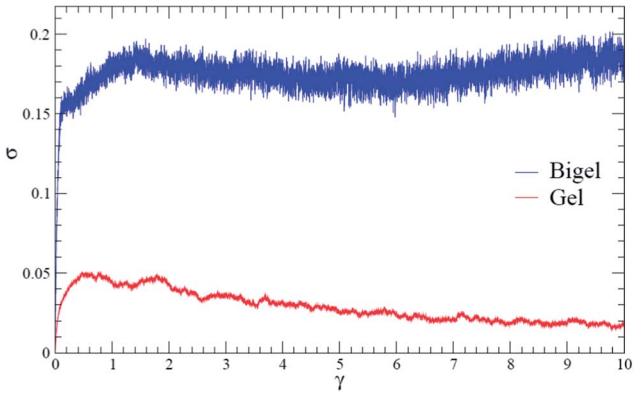

Fig. 10 Average stress *vs.* strain curves for realisations of the 1CM (gel) and the symmetric 2CM (bigel, $c = 0.5$) at $\phi_{\mathrm{tot}} = 0.10$ and $N_{\mathrm{tot}} = 5 \times 10^4$. The 2CM appears stiffer (at low values of the strain), has a higher yield stress (the stress has a higher peak in the 2CM) and retains higher stress at high values of the strain γ.

This observation is confirmed by the cluster analysis in Fig. 12, where the total number of particles of a certain species belonging to clusters of a given size, is plotted as a function of the strain γ. At low γ, a large fraction of the particles clearly belongs to a single cluster. Increasing the value of γ leads to a rearrangement of the particles, with the particles in the gels (1CM) staying lumped in a single compact cluster, whereas those in the bigel (symmetric 2CM) rearrange into smaller clusters. This behaviour is not due to the more dilute concentration of particles of a given species in the bigel with respect to a gel with the same ϕ_{tot}. In fact, as shown in Fig. 12, this observation is robust even when comparing a 1CM at half the volume fraction of that of the 2CM.

The analysis of the usual $S(k)$, done by using eqn (3) with $b_i = 1$ for all the species, is reported in Fig. 13 for both the gels and bigels. Such an analysis is compatible with the scenario outlined above: upon increasing the strain, at low k the structure factor is significantly higher, whereas in the case of the bigel the low k values remain of the same order of magnitude.

Thanks to these observations, we remark the role played by the presence of a second species with selective interaction. In fact, the bigels are somewhat more "ductile", as they break up

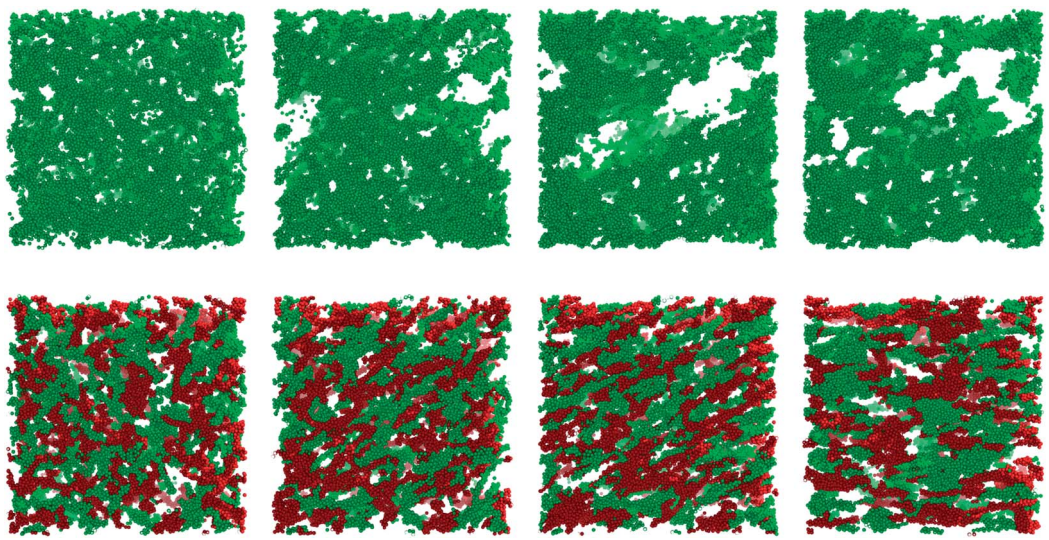

Fig. 11 Sample snapshot for the gel (top row) and bigel (bottom row) at values of the strain $\gamma = 0, 1, 2, 8$ (from left to right). The gel breaks and becomes denser at large values of γ, so that the majority of particles are part of a single large cluster even at large strains. For the bigel, instead, the system breaks up into a large number of smaller clusters (see Fig. 12) that do not coalesce.

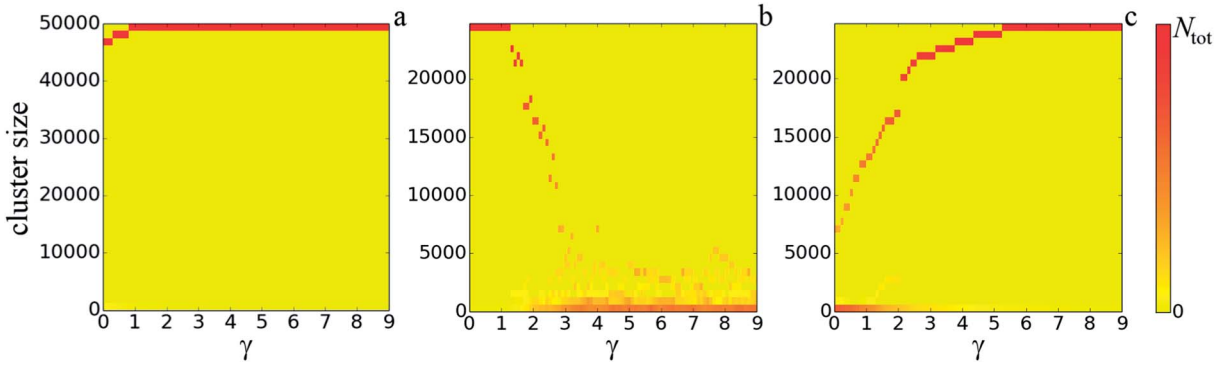

Fig. 12 In this density plot, we show the number of particles belonging to clusters of sizes specified in the ordinates that are found at the different shear strains γ. Thus, a darker color in correspondence with a given size means that the majority of particles belong to clusters of that size. Data refer to (a) a one-component (1CM) sample at $\phi_{tot} = 0.10$ and $N_{tot} = 5 \times 10^4$ particles, (b) a bigel (symmetric 2CM) with an overall volume fraction at $\phi_{tot} = 0.10$ and $N_{tot} = 5 \times 10^4$ particles, and (c) a 1CM sample at $\phi_{tot} = 0.05$ and $N_{tot} = 2.5 \times 10^4$ particles. The vertical axis indicates the cluster size, and the number of particles belonging to a cluster of a given size is encoded in the color scale. At strain $\gamma = 0$ both the 2CM and 1CM show a large cluster that contains the majority of the particles of the sample of the given species. As strain is increased, the 2CM breaks up into smaller clusters, whereas a single, large, compact cluster withstands large strain values in both the 1CM cases.

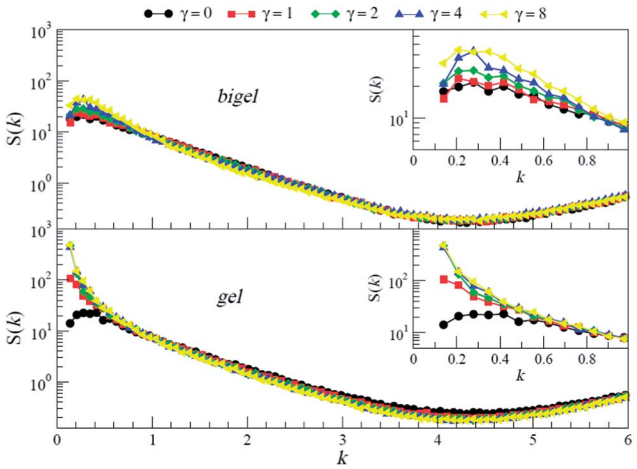

Fig. 13 Structure factor for the arrested 1CM (gel) and 2CM (bigel), at different values of strain γ, averaged over 8 samples. The signal of $S(k)$ increases much more significantly at low k for the gel, confirming that in this case the structures formed upon deformation have a larger characteristic length-scale than those of the bigel. In the corresponding insets, a magnified version of the same data emphasises the separation in the low k signal.

into a structure made of clusters that flows plastically. This determines the capability of the bigels of better sustaining large strain deformations with respect to their 1CM counterparts. In addition, one can speculate on the fact that if the deformation was reversed, neither the gel nor the bigel will "heal". It is hard to think that the deformation reversal will even partially lead to the reformation of a percolating structure in either case. What we expect is that, upon strain reversal, particles of the one-component gel will form a compact cluster and those in the multi-component gel a gas of clusters.

5. Conclusions

In this paper, we have discussed several aspects of bigels, a new form of colloidal gels that results from an arrested demixing of two colloidal species.[1] In particular, by using the scaling proposed by Furukawa, we have shown how the kinetics of bigel formation is compatible with that of an arrested spinodal decomposition driven by demixing.[24,25] This observation strengthens the idea that the arrested phase-separation paradigm of colloidal gelation can be extended to binary mixtures. With the use of computer simulations we have investigated the *phase diagram* of bigels. As expected, at equal molar fraction, $c = 50\%$, and sufficiently large volume fractions ϕ_{tot}, a bigel is always obtained as a result of a deep quench into the two-phase region. For moderate asymmetry of the composition c, a bigel is also obtained, but when the asymmetry becomes large enough, then only the dominant component forms a gel, while the other forms small clusters trapped into the pores left by the gel.

The experimental realisation of bigels requires a control of the interspecies interaction between the different colloidal species. We have achieved this experimentally by using DNA-coated colloids (DNACCs) that allow implementation of programmable interactions encoded into the DNA sequences. While this is not the only route that can be envisaged, DNACCs have the advantage that the attraction is temperature activated and rises very sharply when quenching below a given melting temperature, due to the large amount of DNA strands mediating the interactions.[44,47,48,57] Moreover, the bonding is fully reversible and a system can be brought back to the initial state by setting the temperature above the melting temperature. We have investigated the non-symmetric case and found a semi-quantitative agreement with the computer simulations. In particular, the transition from a bigel to a single gel is confirmed by increasing the concentration of a species with respect to the other. In addition, an interesting issue to address is the nature of the packing in the arms of the bigels. As a matter of fact, it has been recently shown that crystallization can occur in the branches of gels if the range of the potential is varied.[58,59] In the present case, the range of the potential is too short to allow rearrangements that would generate crystalline structures. In the experiments, the interactions between the DNA strands probably inhibit crystallization.

The differences in nature between the gels and the bigels are reflected by their mechanical properties, of which our stress–strain analysis represents a clear indication. A bigel appears to be more resistant to strain than a gel at the same volume fraction. This important property is a consequence of the steric repulsion between the branches made of different components. For example, we show (Fig. 10) for $\phi_{tot} = 0.1$ that the stress at the yield point is about four times larger for a bigel than for the gel. Moreover, above the yield point, a one-component gel compactifies and the stress rapidly relaxes, while the bigel attains a stationary state where the stress remains basically constant. Inspection of the microscopic rearrangements suggests that, after a first strain-induced breakup of the percolating structure, steric repulsion between the two species of the bigels prevents further demixing and compactification that would otherwise lead to a complete failure, as for the case of the one-component gels. These preliminary results suggest that one could expect bigels to show quite unusual mechanical properties.

We have now proven beyond doubt that bigels can be obtained in experiments and that computer simulations can offer a valuable guiding tool. In this paper we have discussed the kinetics that characterises the arrested demixing, which provides an interesting route that suggests new exploring directions. For example, the interplay between the typical diffusion time and the association/dissociation rate could be used in this model system to design new materials. Different smart structures can be assembled by playing with kinetic arrest. Recently, in fact, we have produced core–shell gels assembled by imposing a properly devised temperature history to the samples.[26] This was just a first example of how the sharp thermal activation of DNA-mediated interactions[44,47,48,57] can be used to selectively melt (or assemble) one species at a time, exploiting thereby a kinetic self-assembly procedure to construct structures with a higher degree of complexity.

The self-assembly strategy we propose allows an unprecedented control over the morphology of multi-component mesoporous materials and can find future application in all the instances where a well defined phase separation at the micro- or nano-scale is required. This is the case, for example, of hybrid photovoltaics in which mesoporous silicon scaffolds coexist with a polymeric component.[60] Similarly, electron and ion transport in modern Li-ion batteries can be optimized by controlling the structure of nanoporous electrodes.[61] We also envisage the application of multi-component colloidal gels in the manufacture of amorphous photonic materials that mimic the sponge-like phases providing structural coloring in some species of birds[62–65] and beetles.[66] These biological materials are thought to be assembled *via* arrested phase separation of keratin or chitin and could be mimicked by carefully controlling the arrested spinodal decomposition in colloidal mixtures, with the additional possibility of tuning the photonic response by using multiple components with different refractive indices.

In recent years, there have been great advances in the synthesis of particles with special shape and directional interactions, with the idea of using them as the fundamental step of a bottom-up approach in which microscopic complex building blocks are designed to obtain macroscopic complex systems.[67–70] The introduction of directionality mimics the interactions in molecular systems. In this sense the passage from spherically symmetric to directional colloids is seen as the passage from atomic to microscopic systems so that patchy colloids can be seen as colloidal molecules.[67] While this is a really promising area of investigation, it has also some important limitations. Most of the time, the synthesis of patchy colloidal particles is a very delicate process with a certain degree of uncertainty. Moreover, it is hard to foresee, for the moment, a method that could achieve a high throughput. Here we propose a different paradigm to the self-assembly of complex structures. In the case discussed here, the building blocks are simple spherically symmetric particles with isotropic interactions. In principle, they are simple to produce in great quantity in a reproducible way. The complexity comes into play, in our case, in considering a binary mixture in which we play with the specificity of the interactions, thus offering a robust approach to self-assembly. Such a general approach, based on both kinetics and thermodynamics, could be easily applied to systems of different nature and size and its simplicity should make the assembly process capable of sustaining a certain degree of impurity.

Moreover, we do not have to be limited to binary mixtures. It is possible to envisage different self-assembled structures once we consider a large number of components. In this case the control parameter space would increase dramatically as well as the number of target structures that could be achieved. It is clear, however, that by considering a larger number of colloidal species in order to obtain n-component gel-like systems (with $n > 2$), the joined theoretical and computational tools will play an even more crucial role in guiding the experiments. In this sense, the present study represents an example of the typical integration between theory/simulations and experiments that we believe will be fundamental for this new kind of systems.

Acknowledgements

DF, FV, and GF acknowledge support by the SNSF (grants PP0022_119006 and PP0022_140822/1). LD acknowledges support from the Marie Curie ITN-COMPLOIDS grant no. 234810, the Cambridge NanoDTC, the Ernest Oppenheimer Fund and the Emmanuel College. EE thanks the Winton program for Sustainable Energy for funding.

References

1 F. Varrato, L. Di Michele, M. Belushkin, N. Dorsaz, S. H. Nathan, E. Eiser and G. Foffi, *Proc. Natl. Acad. Sci. U. S. A.*, 2012, **109**, 19155–19160.
2 E. Zaccarelli, *J. Phys.: Condens. Matter*, 2007, **19**, 323101.
3 M. Kolb, R. Botet and R. Jullien, *Phys. Rev. Lett.*, 1983, **51**, 1123–1126.
4 T. Vicsek and F. Family, *Phys. Rev. Lett.*, 1984, **52**, 1669–1672.
5 P. Meakin, *Phys. Rev. Lett.*, 1983, **51**, 1119–1122.
6 A. Hasmy, M. Foret, J. Pelous and R. Jullien, *Phys. Rev. B: Condens. Matter Mater. Phys.*, 1993, **48**, 9345–9353.

7 M. Rottereau, J. C. Gimel, T. Nicolai and D. Durand, *Eur. Phys. J. E*, 2004, **15**, 133–140.
8 M. Rottereau, J. C. Gimel, T. Nicolai and D. Durand, *Eur. Phys. J. E*, 2004, **15**, 141–148.
9 D. A. Weitz and M. Oliveria, *Phys. Rev. Lett.*, 1984, **52**, 1433–1436.
10 M. Carpineti and M. Giglio, *Phys. Rev. Lett.*, 1992, **68**, 3327–3330.
11 A. H. Krall and D. A. Weitz, *Phys. Rev. Lett.*, 1998, **80**, 778–781.
12 L. Cipelletti, S. Manley, R. C. Ball and D. A. Weitz, *Phys. Rev. Lett.*, 2000, **84**, 2275–2278.
13 P. J. Lu, E. Zaccarelli, F. Ciulla, A. B. Schofield, F. Sciortino and D. A. Weitz, *Nature*, 2008, **453**, 499–503.
14 E. Zaccarelli, P. J. Lu, F. Ciulla, D. A. Weitz and F. Sciortino, *J. Phys.: Condens. Matter*, 2008, **20**, 494242.
15 G. Foffi, C. De Michele, F. Sciortino and P. Tartaglia, *J. Chem. Phys.*, 2005, **122**, 224903.
16 V. Testard, L. Berthier and W. Kob, *Phys. Rev. Lett.*, 2011, **106**, 125702.
17 L. Ramos and L. Cipelletti, *Phy. Rev. Lett.*, 2005, **94**, 158301.
18 W. C. K. Poon, *J. Phys.: Condens. Matter*, 2002, **14**, R859.
19 G. Foffi, C. D. Michele, F. Sciortino and P. Tartaglia, *Phys. Rev. Lett.*, 2005, **94**, 078301.
20 K. G. Soga, J. R. Melrose and R. C. Ball, *J. Chem. Phys.*, 1998, **108**, 6026–6032.
21 E. Del Gado, *J. Phys.: Condens. Matter*, 2010, **22**, 104117.
22 P. Levitz, *Adv. Colloid Interface Sci.*, 1998, **76–77**, 71–106.
23 P. Levitz, *Cem. Concr. Res.*, 2007, **37**, 351–359.
24 H. Furukawa, *Phys. A*, 1984, **123**, 497–515.
25 H. Furukawa, *J. Phys. Soc. Jpn.*, 1989, **58**, 216.
26 L. Di Michele, F. Varrato, J. Kotar, S. H. Nathan, G. Foffi and E. Eiser, *Nat. Commun.*, 2013, **4**, 2007.
27 T. Gibaud, N. Mahmoudi, J. Oberdisse, P. Lindner, J. S. Pedersen, C. L. P. Oliveira, A. Stradner and P. Schurtenberger, *Faraday Discuss.*, 2012, 267–284.
28 K. A. Dawson, G. Foffi, F. Sciortino, P. Tartaglia and E. Zaccarelli, *J. Phys.: Condens. Matter*, 2001, **13**, 9113.
29 G. Foffi, G. D. McCullagh, A. Lawlor, E. Zaccarelli, K. A. Dawson, F. Sciortino, P. Tartaglia, D. Pini and G. Stell, *Phys. Rev. E: Stat., Nonlinear, Soft Matter Phys.*, 2002, **65**, 031407.
30 E. Zaccarelli, S. V. Buldyrev, E. La Nave, A. J. Moreno, I. Saika-Voivod, F. Sciortino and P. Tartaglia, *Phys. Rev. Lett.*, 2005, **94**, 218301.
31 W. P. Krekelberg, J. Mittal, V. Ganesan and T. M. Truskett, *J. Chem. Phys.*, 2007, **127**, 044502–044508.
32 M. G. Noro and D. Frenkel, *J. Chem. Phys.*, 2000, **113**, 2941–2944.
33 E. Zaccarelli, G. Foffi, K. A. Dawson, F. Sciortino and P. Tartaglia, *Phys. Rev. E: Stat., Nonlinear, Soft Matter Phys.*, 2001, **63**, 031501.
34 V. Testard, L. Berthier and W. Kob, eprint arXiv:1309.1587, 2013.
35 M. A. Miller and D. Frenkel, *Phys. Rev. Lett.*, 2003, **90**, 135702.
36 J. Largo, M. A. Miller and F. Sciortino, *J. Chem. Phys.*, 2008, **128**, 134513.
37 N. Dorsaz and G. Foffi, *J. Phys.: Condens. Matter*, 2010, **22**, 104113.
38 E. Sch oll-Paschinger and G. Kahl, *J. Chem. Phys.*, 2003, **118**, 7414–7424.
39 J. Bibette, T. G. Mason, H. Gang and D. A. Weitz, *Phys. Rev. Lett.*, 1992, **69**, 981–984.
40 A. K. Thakre, W. K. den Otter and W. J. Briels, *Phys. Rev. E: Stat., Nonlinear, Soft Matter Phys.*, 2008, **77**, 011503.
41 D. G. A. L. Aarts and H. N. W. Lekkerkerker, *J. Phys.: Condens. Matter*, 2004, **16**, S4231.
42 T. Hashimoto, M. Itakura and N. Shimidzu, *J. Chem. Phys.*, 1986, **85**, 6118.
43 T. Hashimoto, *Phase Transitions*, 1988, **12**, 47–119.
44 L. Di Michele and E. Eiser, *Phys. Chem. Chem. Phys.*, 2013, **15**, 3115–3129.
45 S. Angioletti-Uberti, B. M. Mognetti and D. Frenkel, *Nat. Mater.*, 2012, **11**, 518–522.
46 A. J. Kim, P. L. Biancaniello and J. C. Crocker, *Langmuir*, 2006, **22**, 1991–2001.
47 R. Dreyfus, M. E. Leunissen, R. Sha, A. Tkachenko, N. C. Seeman, D. J. Pine and P. M. Chaikin, *Phys. Rev. E: Stat., Nonlinear, Soft Matter Phys.*, 2010, **81**, 041404.
48 R. Dreyfus, M. E. Leunissen, R. Sha, A. V. Tkachenko, N. C. Seeman, D. J. Pine and P. M. Chaikin, *Phys. Rev. Lett.*, 2009, **102**, 048301.
49 M. E. Leunissen, R. Dreyfus, R. Sha, N. C. Seeman and P. M. Chaikin, *J. Am. Chem. Soc.*, 2010, **132**, 1903–1913.
50 M. E. Leunissen, R. Dreyfus, F. C. Cheong, D. G. Grier, R. Sha, N. C. Seeman and P. M. Chaikin, *Nat. Mater.*, 2009, **8**, 590–595.
51 M. E. Leunissen, R. Dreyfus, R. Sha, T. Wang, N. C. Seeman, D. J. Pine and P. M. Chaikin, *Soft Matter*, 2009, **5**, 2422–2430.
52 J.-L. Mergny and L. Lacroix, *Oligonucleotides*, 2003, **13**, 515–537.
53 M. A. Miller and D. Frenkel, *J. Phys.: Condens. Matter*, 2004, **16**, S4901.
54 N. Otsu, *IEEE Trans. Syst., Man, Cybern., Syst.*, 1979, **9**, 62–66.
55 S. Plimpton, *J. Comput. Phys.*, 1995, **117**, 1–19.
56 C. E. Maloney and A. Lemaître, *Phys. Rev. E: Stat., Nonlinear, Soft Matter Phys.*, 2006, **74**, 016118.
57 P. Varilly, S. Angioletti-Uberti, B. M. Mognetti and D. Frenkel, *J. Chem. Phys.*, 2012, **137**, 094108.
58 A. Fortini, E. Sanz and M. Dijkstra, *Phys. Rev. E: Stat., Nonlinear, Soft Matter Phys.*, 2008, **78**, 041402.
59 E. Sanz, C. Valeriani, T. Vissers, A. Fortini, M. Leunissen, A. Van Blaaderen, D. Frenkel and M. Dijkstra, *J. Phys.: Condens. Matter*, 2008, **20**, 494247.
60 A. Nahor, O. Berger, Y. Bardavid, G. Toker, Y. Tamar, L. Reiss, M. Asscher, S. Yitzchaik and A. Sa'ar, *Phys. Status Solidi C*, 2011, **8**, 1908–1912.
61 J. H. Pikul, H. Gang Zhang, J. Cho, P. V. Braun and W. P. King, *Nat. Commun.*, 2013, **4**, 1732.
62 H. Yin, B. Dong, X. Liu, T. Zhan, L. Shi, J. Zi and E. Yablonovitch, *Proc. Natl. Acad. Sci. U. S. A.*, 2012, **109**, 10798–10801.
63 E. R. Dufresne, H. Noh, V. Saranathan, S. G. J. Mochrie, H. Cao and R. O. Prum, *Soft Matter*, 2009, **5**, 1792–1795.
64 D. G. Stavenga, J. Tinbergen, H. L. Leertouwer and B. D. Wilts, *J. Exp. Biol.*, 2011, **214**, 3960–3967.
65 P. F. Damasceno, M. Engel and S. C. Glotzer, *Science*, 2012, **337**, 453–457.

66 B. Q. Dong, T. R. Zhan, X. H. Liu, L. P. Jiang, F. Liu, X. H. Hu and J. Zi, *Phys. Rev. E: Stat., Nonlinear, Soft Matter Phys.*, 2011, **84**, 011915.
67 Y. Wang, Y. Wang, D. R. Breed, V. N. Manoharan, L. Feng, A. D. Hollingsworth, M. Weck and D. J. Pine, *Nature*, 2012, **491**, 51–55.
68 S. Sacanna, M. Korpics, K. Rodriguez, L. Colón-Meléndez, S.-H. Kim, D. J. Pine and G.-R. Yi, *Nat. Commun.*, 2013, **4**, 1688.
69 D. de las Heras, J. M. Tavares and M. M. Telo da Gama, *Soft Matter*, 2012, **8**, 1785–1794.
70 A. Goyal, C. K. Hall and O. D. Velev, *Soft Matter*, 2010, **6**, 480–484.

